Electronic Supplementary Material (ESI) for Journal of Materials Chemistry A.
This journal is © The Royal Society of Chemistry 2021

Supplementary Information

Templating Synthesis of Natural Cotton-based Hierarchically Structured Carbon Hollow Microfibers for High-performance Solar Vapor Generation

Shijun Lei, Dali Huang, Shuhao Liu, Mingfeng Chen, Rong Ma, Minxiang Zeng, Dan Li, Wenchao Ma*, Ling Wang* and Zhengdong Cheng

S1. Supplementary Methods

S1.1 Materials

Cotton fabrics as raw materials that used in this study were purchased from VWR company (USA, 100% pure cotton). A piece of cotton fabric was 100 mm diametric with an approximate thickness of 5 mm. Those cotton fabrics were made from natural cotton microfibers and presented white, soft, bushy-haired and flexible properties.

S1.2 Freezing-induced fabrication procedure

For the preparation of HCMFs 1, a piece of cotton fabric was first purified by immersing into 1 L DI water for 6 h to remove residuals that produced during the weaving process (Fig. S1a, b). After drying in an oven at 50 ^{o}C overnight, the CMFs were wrapping with an aluminum sheet tightly and moved into a furnace (Thermo Fisher Scientific). Then, controlled carbonization was proceeding at 400 ^{o}C for 1.5 h with a heating rate of 10 ^{o}C/min (Fig. S1c). After cooling down to ambient temperature in the air (approximate 3 h), the products were taking out from the aluminum sheet and immersed in 1 L of DI water. The water in the fiber-water mixtures was cycling in a water circulator for 6 h to remove unreacted residuals and moisten the fiber

core with water adequately (Fig. S1d). Finally, the HCMFs 1 was achieved after freezing dry the products in a freeze dryer at -50 ^{o}C for 48 h (Fig. S1e, f).

Note that the aluminum sheet had the function of over oxidation protection and splashing prevention for the CMF samples during controlled carbonization process. After controlled carbonization process, the fiber core decomposed while carbon skeletons remained and hollow channel structures were initially formed in the carbon fibers.[1-2] These hollow channels were filled by water in the water cycling process and further enhanced by expansion effect of water-to-ice during freeze-casting process. After ice sublimation in the freezing-dry process, the high-performance HCMFs solar vapor generator was finally achieved (Fig. 1b).

For the preparation of the CMFs 2 and the HCMFs 2, the original CMFs and the as-prepared HCMFs 1 were treated with O_2-plasma for 2 min to 3 min in a plasma cleaner (PDC-32G) to further increase the hydrophilicity, respectively.

S2. Supplementary Figures

S2.1 Introducing of freezing-induced construction process for HCMFs solar vapor generator

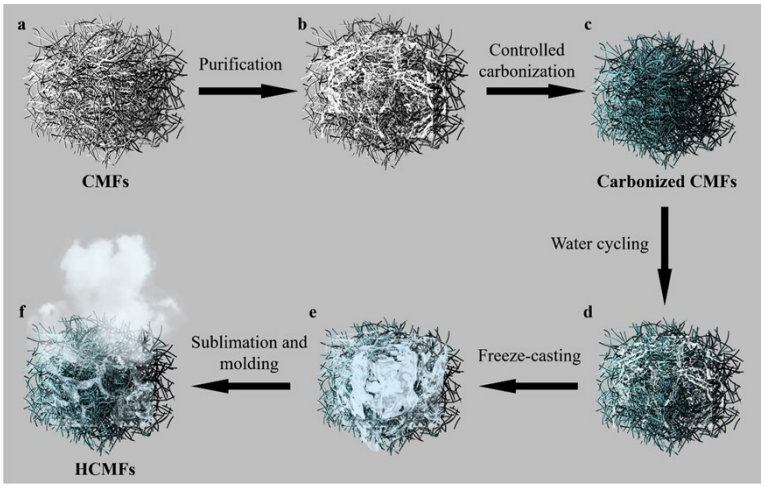

Fig. S1 Schematics of freezing-induced construction process for preparation of the high-performance HCMFs solar vapor generator. The construction process was consisted by purification, controlled carbonization, water cycling, freeze-casting, and sublimation and molding processes. (a) original cotton microfibers, (b) cotton microfibers purified by DI water, (c) carbonized cotton microfibers, (d) carbonized

cotton microfibers purified by DI water, (e) enhancing hollow channel structures in the fibers by freeze-casting, (f) the HCMFs solar vapor generator.

S2.2 Introducing of HCMFs solar vapor generator

The freezing-induced construction process made hollow channels inside the cotton fibers, combined with bundle gap and inter-fiber spacing, the HCMFs solar vapor generator exhibited excellent vapor generation performance. It is worth to mention that, cotton fibers exhibited different morphologies during growth cycle. As shown in Fig. S2, after cotton seeds peeped out from the ground in the seedling period, cotton blossoms bloomed during flower stage, and further become cotton bolls after faded. The initial cotton bolls contained abundant cotton fibers with hollow structures. These hollow structures named “lumen” played an important role in water and nutrition transportation to sustained the fast growth of cotton bolls via transpiration. But after cracking, the cotton bolls eventually ceased growing, the transpiration function of lumen was not needed anymore. So, the lumen was collapsed and closed to prevent extra water and nutrition loss from lumen transpiration, forming twists and convolutions of the cotton fibers.

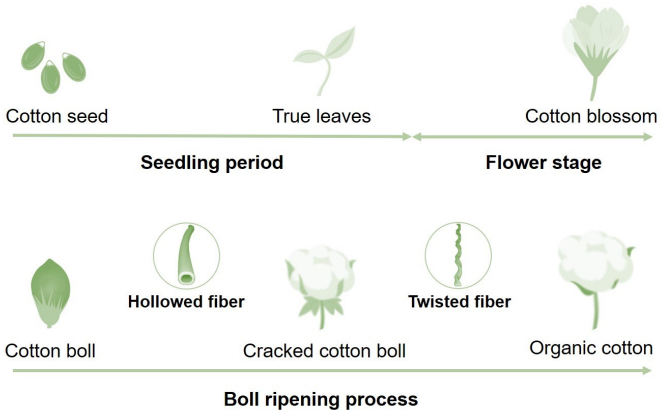

Fig. S2 Growth cycle and fiber formation of cotton.

As the cotton pad used in this paper was made from matured cotton fibers, the fiber lumens were already collapsed. A large amount of pristine cotton fibers (CMFs) was showed non-

hollowed structure in the SEM image in Fig. S3a (yellow dashed circles). The twists fibers showed in Fig. S3b (yellow dashed lines) was formed because of the collapse and close of the fiber lumen, which again evidenced non-hollowed structure of the cotton fibers. Fig. S3c showed that the CMFs was formed by ribbon-shaped twisted fibers with non-hollowed structure (yellow dashed circles). The non-hollowed structure of a single fiber in the CMFs could be clearly seen in the inset image with high magnification. During freezing-induced construction process, the cotton fibers were expanded and loosened fiber twists, forming hollowed channels inside. The SEM image in Fig. S3d demonstrated hollowed structure of the fibers (yellow dashed circles) expanded by means, these holes or cracks were irregular shaped, but were significantly different with the pristine cotton fibers.

It is worth mentioning that, the observed “solid” structure of the pristine cotton fibers was because of the collapse and close of the fiber lumen, but not intrinsic “solid”, our structural engineering was more like a lumen reopening process. These reopened lumens served as crucial water pathways and enhanced water transport performance by providing additional capillary pumping channels and augmenting water diffusion, reduced vaporization enthalpy by meniscus thin-film evaporation. Combined with bundles and inter-fiber water pathways, the HCMFs solar evaporator exhibited an extreme high water evaporation rate and a high energy efficiency.

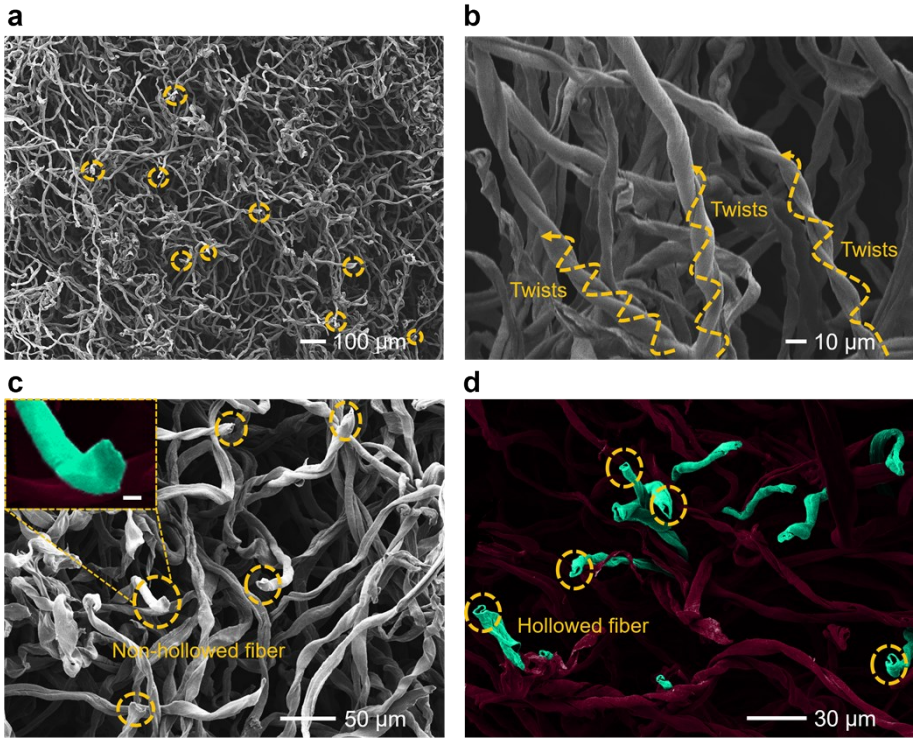

Fig. S3 SEM images of (a) large amount of pristine cotton fibers (non-hollowed structure of the fibers were marked by yellow dashed circles), (b) twists fibers in the CMFs (yellow dashed lines), (c) non-hollowed structure of the fibers in the CMFs (yellow dashed circles, the inset image showed the non-hollowed structure of a single fiber in the CMFs with high magnification, the corresponding scale bar was 5 μm), (d) hollowed structure of the fibers in the HCMFs (yellow dashed circles).

To evaluate the hollow structure before and after freezing-induced construction process, the radial areas of the fibers were measured, and the expansion ratio of the holes was then calculated. Given that the radial areas of fibers changed after freezing-induced construction process was because of the expansion of holes, radial areas of fibers were used to calculate the expansion ratio of holes (because the holes in the CMFs could barely observed and difficult to measure). The radial areas (measured by Image-J software via particle analysis method) and the corresponding equivalent radii of non-hollowed fibers in the CMFs (Fig. S3c) and hollowed fibers in the HCMFs (Fig. S3d) were showed in Table S1.

The equivalent radius was calculated by the formular below:

$$R_{eqv} = \sqrt{\frac{S_F}{\pi}} \quad \text{(S1)}$$

The expansion ratio of holes was calculated by the following formular:

$$\varepsilon = \frac{\sum_{i=1}^{5} R_{eqv,HCMFs,i} - \sum_{i=1}^{5} R_{eqv,CMFs,i}}{\sum_{i=1}^{5} R_{eqv,CMFs,i}} \times 100\% \quad \text{(S2)}$$

Where S_F was the radial area of fiber, R_{eqv} was the equivalent radius, ε was the expansion ration of holes, $R_{eqv,CMFs}$, $R_{eqv,HCMFs}$ represented the equivalent radius of non-hollowed fiber of the CMFs and hollowed fiber of the HCMFs, respectively.

Table S1. Radial areas and equivalent radii of fibers of CMFs and HCMFs

No.	$S_{F,\ CMFs}$ (μm^2)	$R_{eqv,\ CMFs}$ (μm)	$S_{F,\ HCMFs}$ (μm^2)	$R_{eqv,\ HCMFs}$ (μm)
1	16.264	2.275877	45.507	3.806925
2	23.118	2.713378	61.226	4.415736
3	80.605	5.066595	91.014	5.383804
4	77.638	4.972472	83.806	5.166218
5	33.551	3.268797	70.345	4.733167
Average		3.659424		4.70117

The expansion ratio was calculated to be 28.5%, which demonstrated a successful expansion of holes inside the cotton fiber after freezing-induced construction process.

After freezing-induced construction process, most of the fibers of the HCMFs were become hollow. These hollow channels inside the fiber provided crucial water pathways during solar evaporation and desalination process. To evaluate the performance of the freezing-induced construction process, the hollow rate was estimated by the following formular:

$$\varepsilon_{hr} = \frac{N_h}{N_h + N_s} \times 100\% \quad \text{(S3)}$$

Where ε_{hr} was the hollow rate, N_h was the number of the hollowed fibers in the HCMFs, N_s was the number of the non-hollowed fibers in the HCMFs.

The number of the hollowed fibers and the non-hollowed fibers in the HCMFs were counted in a SEM image which contained a large number of cross section structure of the fibers. As seen in Fig. S4, the number of hollowed fibers (green colored) was counted to be 22, and the number of non-hollowed fibers (yellow colored) was counted to be 4. The hollow rate of the HCMFs was approximately to be 85%.

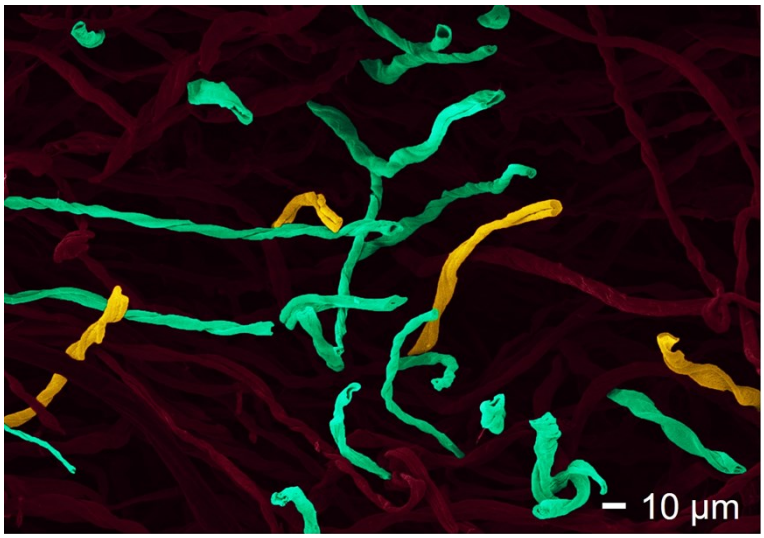

Fig. S4 SEM image of hollowed (green colored) and non-hollowed (yellow colored) fibers in the HCMFs.

S2.3 Solar absorption and mass loss of the HCMFs evaporator during fabrication process

As seen in Fig. S5, after freezing-induced construction process, the white natural cotton pad become black, indicating a reflection decrease of the HCMFs. The solar absorption of the HCMFs was significantly enhanced in comparison with that of the CMFs (Fig. 3c).

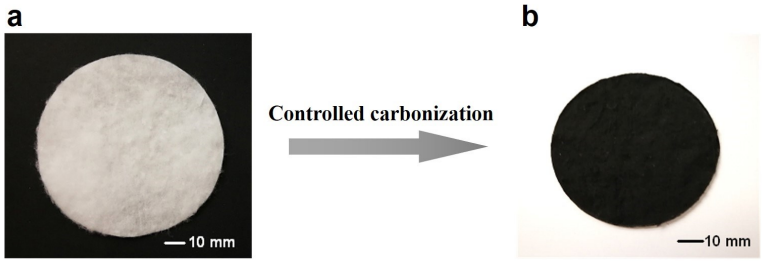

Fig. S5 Images of (a) original cotton fabric that made by natural cotton microfibers, (b) high-performance solar vapor generator with hollow carbonized cotton microfibers.

Due to the carbonization decomposition, the initial 100 mm diametric cotton pad was shrunk into an approximate 70 mm diametric carbon membrane with a thickness of 0.3 mm. The mass change before and after fabrication procedure was presented in Fig. S6 (original cotton microfibers before and after O_2-plasma treatment, hollow carbonized cotton microfibers before and after O_2-plasma treatment were designated as CMFs 1, CMFs 2, HCMFs 1, and HCMFs 2), the residual mass of CMFs 1 and CMFs 2 were essentially the same and similar situation happened in HCMFs 1 and HCMFs 2, indicating O_2-plasma treatment had no significant effect on mass change. But residual mass of CMFs 1 and HCMFs 1 (as well as CMFs 2 and HCMFs 2) was significantly changed, indicating the decomposition of organics were mainly occurred during controlled carbonization process. The weight of HCMFs 1 decreased to 20.2% in comparison with CMFs 1, and the mass loss rate was reached up to 79.8%.

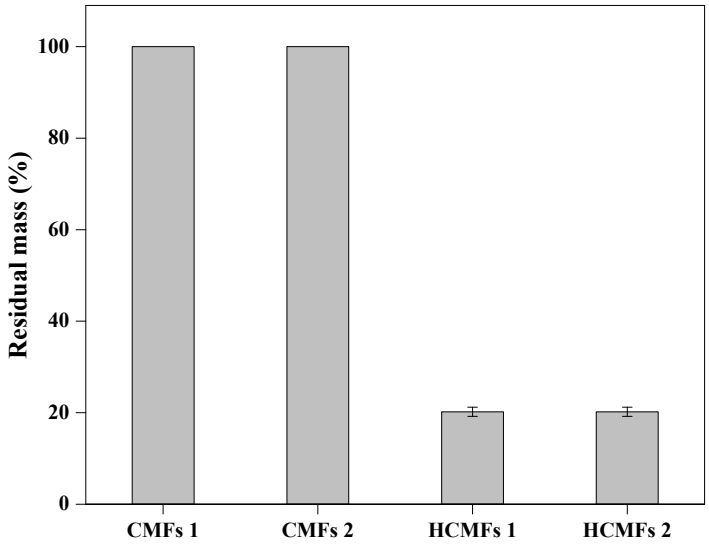

Fig. S6 Mass change of CMFs 1 (original cotton microfibers), CMFs 2 (cotton microfibers with O_2-plasma treatment), HCMFs 1 (hollow carbonized cotton microfibers), and HCMFs 2 (hollow carbonized cotton microfibers with O_2-plasma treatment) during construction processes.

S2.4 Flexibility of HCMFs

The as-prepared HCMFs evaporator was black, lightsome, soft, and flexible. During the bending test (Fig. S7a) with a bending radius of 0.5 cm and the compression test (Fig. S7b) with a weight loading of 200 grams, the HCMFs showed good condition without any visible damage. The results demonstrated a certain mechanical stability of the HCMFs.

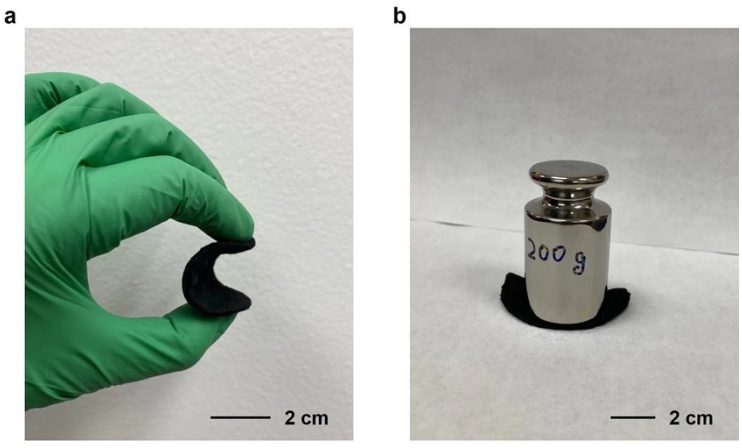

Fig. S7 Photographs of (a) bending and (b) compression test of HCMFs samples.

S2.5 Water transport behavior of CMFs and HCMFs

The water transport behavior was carefully tested by saturated water content and half swollen time. Before testing, the CMFs 1, CMFs 2, HCMFs 1, HCMFs 2 samples were dried in an oven at 50 ^{o}C for 48 h to ensure the samples were fully dried. Then, these samples were contacted with water surface slowly and time-dependent water content of attraction was carefully recorded by a balance. As seen in Fig. S8, the saturated water content of the CMFs 1and the CMFs 2 were 15.6 g g^{-1} and 15.8 g g^{-1}while in the HCMFs 1 and the HCMFs 2 they were 23.7 g g^{-1} and 23.5 g g^{-1}, respectively. Results showed that after construction process, the water attraction of HCMFs samples were significantly increased in comparison with CMFs samples, indicating a structure-dependent water transport was formed in the samples. The hollow-fiber structure of the HCMFs increased equivalent porosity and affected water absorption ability significantly. Although O_2-plasma treatment had no effect on saturated water content, the half-swollen time greatly decreased due to the increase of hydrophilicity (Fig. 3a).

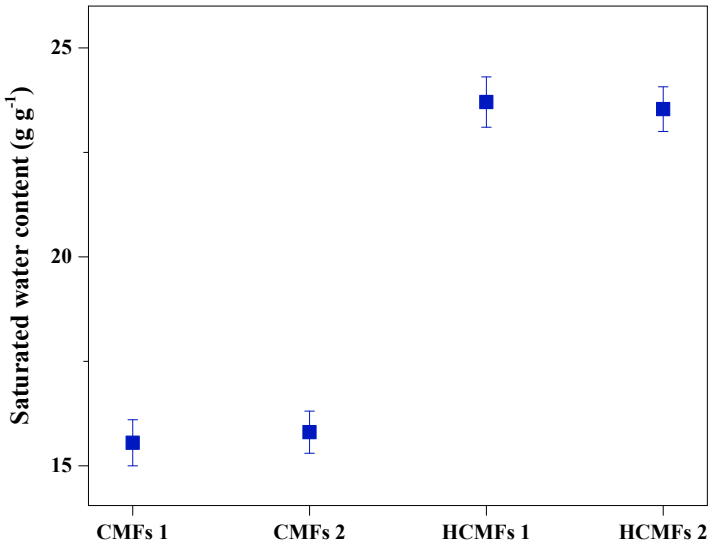

Fig. S8 Water transport behavior. Saturated water content of CMFs 1, CMFs 2, HCMFs 1, and HCMFs 2, respectively.

S2.6 Laboratory water evaporation rate measurement

HCMFs solar evaporator

The solar evaporator was a typical isolation system including HCMFs materials for solar spectrum absorption and light-to-heat conversion, PS foam 1 for heat management to prevent heat loss to the bulk water, and paper wick for water supply. The PS foam 1, the HCMFs materials, and the paper wick were installed on the top of a beaker with seawater (seen in Fig. S9).

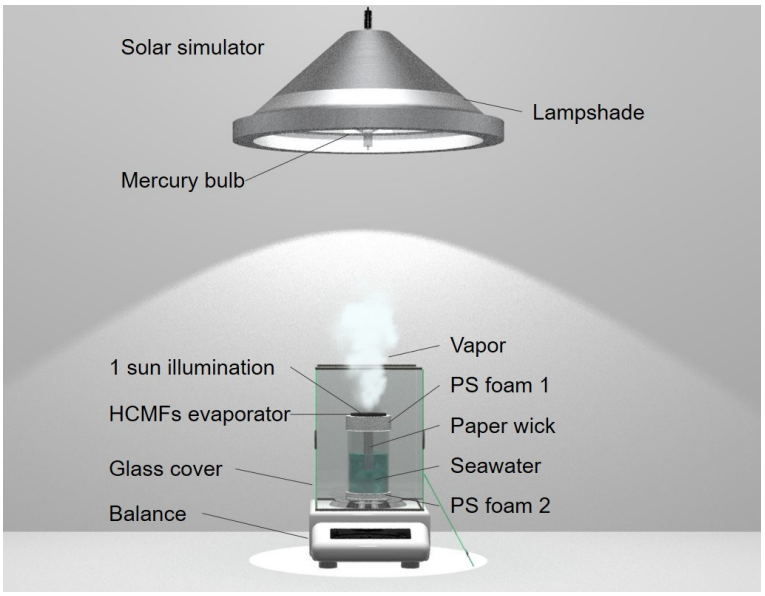

Fig. S9 Schematic illustration of laboratory test of water evaporation based on HCMFs solar vapor generation system.

Laboratory evaporation rate testing system

The above HCMFs solar evaporator was conducted on a balance to record real-time weight loss of water. The top glass shield of the balance was removed to guarantee the fast vapor spreading to the surroundings, which played an important role in sustaining a fast evaporation rate. Given that under 1 sun irradiation, the weighing pan of the balance would be heated. To insulate the extra heat transfer from the weighing pan to the water, the PS foam 2 was inserted between the beaker and the weighing pan of the balance (Fig. S9). The whole system was fenced by wallpaper to prevent extra evaporation by air convection in the lab. The weight loss of water was calculated by the following formular:

$$\Delta m = \frac{dm}{dt} \tag{S4}$$

Where Δm was the weight loss of water, $\frac{dm}{dt}$ was determined by real-time weight change data from the balance.

The evaporation rate was calculated by the formular below:

$$\dot{m}_v = \frac{\Delta m}{S_{HCMFs}} \tag{S5}$$

Where $\dot{m}_v$ was the evaporation rate of water, S_{HCMFs} was the evaporation area.

Given that the evaporation was occurred on the surface of the HCMFs, the evaporation area was equaled to the area of HCMFs material. The value of evaporation area would affect evaporation rate significantly. To measure the evaporation area more accurately, the image of HCMFs was analyzed by particles analysis method using *Image-J* software (Seen in Fig. S10).

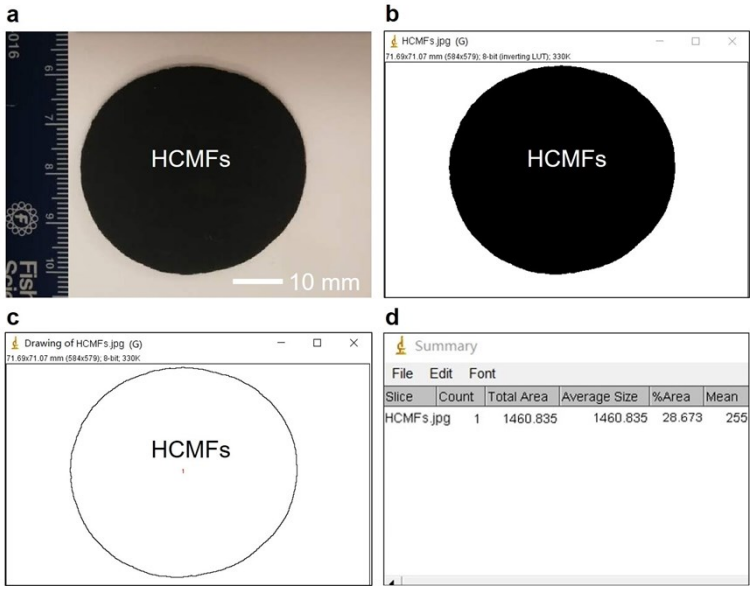

Fig. S10 Evaporation area measurement. (a) Image of the HCMFs with a ruler. (b) Image processing, (c) drawing of the HCMFs, (d) test results by *Image-J* software.

Solar illumination measurement

The solar simulator was made by USHIO, Japan, including a lampshade, a mercury bulb, and a

power supply (Fig. S9). The wavelength of the spectrum was mainly focused from 200 nm to 800 nm. As seen in Fig. S11, the spectral distribution was stronger in ultraviolet region and weaker in infrared region in comparison with atmospheric solar illumination (AM 1.5 G, seen in Fig. 3c).

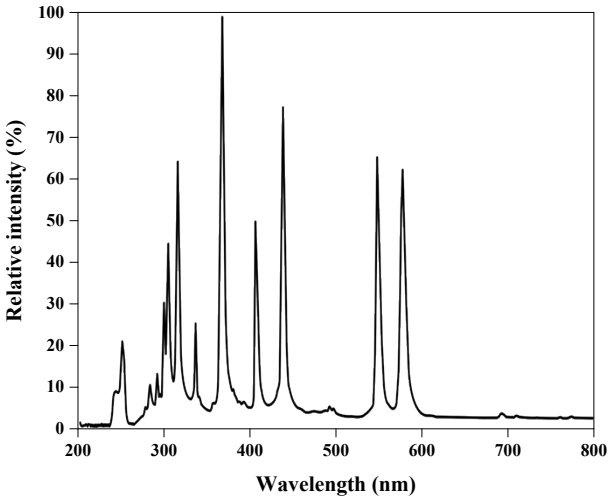

Fig. S11 Spectral distribution of the solar simulator used in laboratory test.

The power intensity of solar illumination was measured by a solar meter (SPM 72). It is worth mentioning that irradiation from the solar simulator in this paper which received by the HCMFs was unequally distributed. As seen in Fig. S12, in a typical solar irradiation area, the highest power density existed at the focus of the circle, then decreased fast in the radial direction. The far from the focus the less of the power density. The power density with distance of 0 mm, 6 mm, 12 mm, 18 mm, and 24 mm from the focus were measured (as seen in Table S2). Results showed that the average solar power density $P_{L0,\ average}$, $P_{L1,\ average}$, $P_{L2,\ average}$, $P_{L3,\ average}$, $P_{L4,\ average}$, were 1352 W m^{-2}, 1244 W m^{-2}, 1022 W m^{-2}, 914 W m^{-2}, and 792 W m^{-2}, respectively.

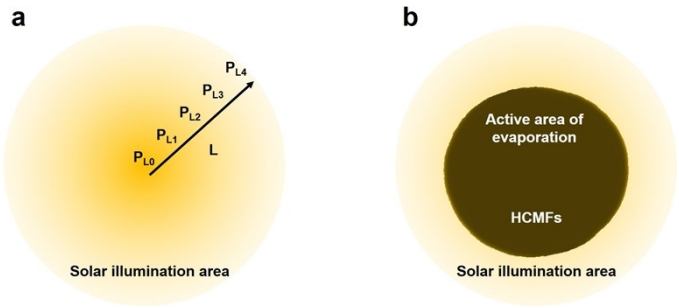

Fig. S12 Schematic images of (a) solar illumination area, (b) active area of evaporation.

Table S2. Solar illumination measurement

No.	L (mm)	P_1 (W m^{-2})	P_2 (W m^{-2})	P_3 (W m^{-2})	$P_{L, average}$ (W m^{-2})
0	0	1354	1350	1353	1352
1	6	1235	1251	1245	1244
2	12	1018	1016	1033	1022
3	18	909	907	927	914
4	24	780	796	799	792

Liner fitting results in Fig. S13 demonstrated that the distance from the focus (*L*) and the power density *P* satisfied the following equation:

$$P(L) = 1354.8 - 24.1667 \times L \quad \text{(S6)}$$

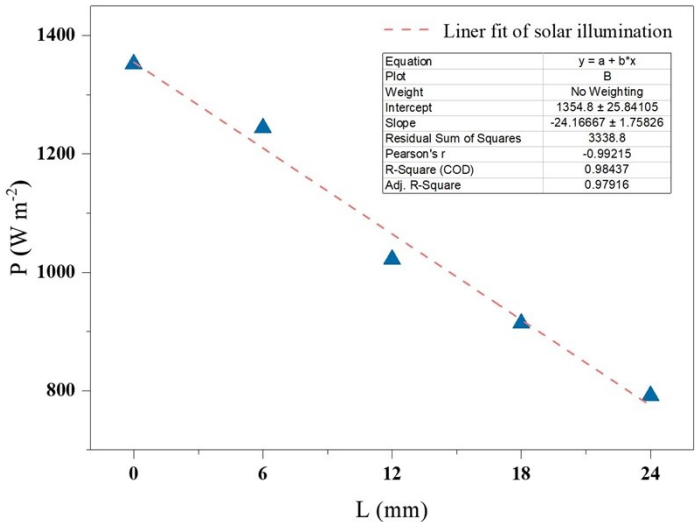

Fig. S13 Liner fitting of the solar illumination

As the active evaporation area was equaled to the HCMFs area that measured by *Image-J* software in Fig. S10, the total solar energy which received by the HCMFs was calculated by the formular below:

$$E = \int_0^{r_{eqv}} 2\pi L P_{(L)} dL \tag{S7}$$

Then the average solar power density on the HCMFs was calculated as follows:

$$P_{in} = \frac{1}{\pi r_{eqv}^2} \int_0^{r_{eqv}} 2\pi L P_{(L)} dL \tag{S8}$$

Where E was the total solar energy that received by the HCMFs solar evaporator, P_{in} was the solar power density on the HCMFs solar evaporator, r_{eqv} was the equivalent radius of the HCMFs solar evaporator.

Calculation results showed that r_{eqv} was equaled to 21.564 mm, and P_{in} was approximated to be 1 kW m^{-2}.

It is worth mentioning that the evaporation rate of 3.2 kg m^{-2} h^{-1} that was achieved in this paper could attribute to (1) the hierarchical water pathways forming by bundles, inter-fiber

spacing, and hollow channels that guaranteed rapid water replenishment by enhancing capillary pumping and water diffusion in the evaporator, (2) the good solar absorption that realized by reducing reflection of the cotton fibers via controlled carbonization, (3) rational thermal management that avoided extra heat loss to the environment, (4) reduced vaporization enthalpy that driven by capillary effect through meniscus thin-film evaporation in the hollow channels.

S2.7 Evaporation rate of artificial Baltic Sea, World Sea, and Dead Sea

The salinity of artificial seawater (from Carolina) was 3.5 % which equaled with salinity of World Sea. Baltic Sea with salinity of 0.8% was acquired by diluting the artificial seawater with DI water and the Dead Sea with salinity of 10% was obtained by concentrating the artificial seawater via water evaporation.[3] As seen in Fig. S14, the mass of artificial seawater with salinities of 0.8% (Baltic Sea), 3.5% (World Sea), and 10% (Dead Sea) were decreased uniformly and rapidly during 3600 s` testing. The evaporation rate was calculated to be 3.2 kg m^{-2} h^{-1}, 3.0 kg m^{-2} h^{-1}, and 2.8 kg m^{-2} h^{-1}, respectively (see Fig. 5a). The evaporation rates were not significantly affected by increasing of the salinities, the water transport behavior was affected by the increasing of salinities that leading to a slight decrease of evaporation rate for World Sea and Dead Sea.

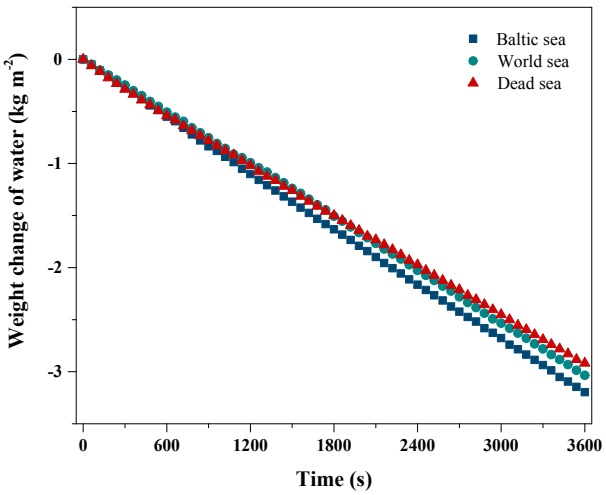

Fig. S14 Weight change of seawater with salinities of 0.8% (Baltic Sea), 3.5% (World Sea), and 10% (Dead Sea) during water evaporation process by the HCMFs 2 solar evaporator.

S2.8 Temperatures of bulk seawater and HCMFs 2 evaporator surface during solar evaporation process

The temperatures of HCMFs 2 surface and the bulk seawater were showed in Fig. S15 For Baltic Sea, World Sea, and Dead Sea, the temperatures on the HCMFs 2 surface were rapidly increased above 50 ^{o}C in 300 s while the bulk seawater remained below 30 ^{o}C during 3600 s evaporation process. The results indicated an efficient light-to-heat conversion of the HCMFs, proved an effective interfacial heating and a successfulness of the thermal isolation of the HCMFs solar vapor generation system. [4-5]

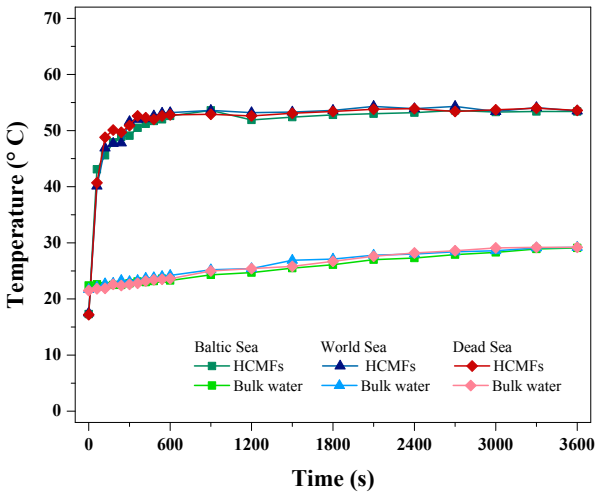

Fig. S15 Temperature change of bulk water (Baltic Sea, World Sea, and Dead Sea) and HCMFs evaporator surface during solar evaporation process.

S2.9 Enthalpy measurement of the HCMFs

The enthalpy of the pure water and the HCMFs were carefully measured by evaporation of water in petri-dish in dark environment. The samples were placed in a sealed incubator where there is no convection and the temperature was carefully controlled at 23°C. The evaporation rate of pure water and water in the HCMFs were measured by continuously tracking mass change of water in 50 h. The water evaporation rate of pure water and water in the HCMFs were showed in Table S3, in the dark environment, the mass change of water in the HCMFs was significantly different from pure water, indicating a structure-dependent evaporation enhancement of the HCMFs materials. The evaporation rate of pure water and water in the HCMFs were subject to a linear relation $y = ax$, where the slope a was the dark evaporation rate (see Fig. S16a, b).

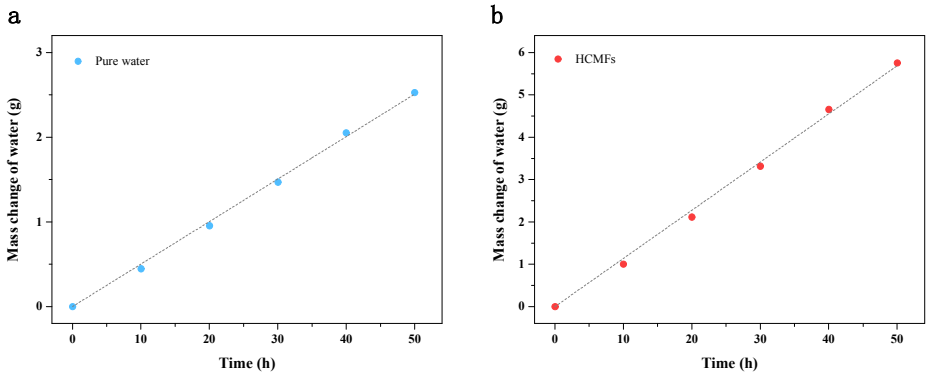

Fig. S16 Liner fitting of evaporation rate of (a) pure water and (b) water in the HCMFs under dark environment.

In the dark environment, the evaporation of pure water and water in the HCMFs were happened spontaneously and the energy for both pure water evaporation and water evaporation in the HCMFs were the same, the enthalpy of water in the HCMFs was calculated by formula below:[6]

$$P_{in} = E_{purewater} \cdot \dot{m}_{purewater} = E_{HCMFs} \cdot \dot{m}_{HCMFs} \quad \text{(S9)}$$

Where P_{in} was energy input, $E_{purewater}$ was water enthalpy which equals to 2256 J g^{-1}, $\dot{m}_{purewater}$ was evaporation rate of pure water, E_{HCMFs} was water enthalpy in the HCMFs, $\dot{m}_{HCMFs}$ was evaporation rate of water in HCMFs. So, the equivalent enthalpy of water in the HCMFs could be calculated by the derived formula:

$$E_{HCMFs} = \left(E_{Purewater} \cdot \dot{m}_{Purewater}\right) \div \dot{m}_{HCMFs} \quad \text{(S10)}$$

Results were showed in Fig. 3b, the equivalent enthalpy of the HCMFs was calculated to be 1066 J g^{-1} which explained the reason of the structure-dependent increasing of water evaporation rate.

Table S3. Mass change of pure water and water in the HCMFs under dark environment

Time (h)	Evaporation rate of pure water (kg m^{-2})	Evaporation rate of HCMFs (kg m^{-2})	Temperature (^oC)
0	0	0	23
10	0.446340239	1.000328742	23
20	0.953740239	2.115908282	23
30	1.469567817	3.315798782	23
40	2.051767258	4.656957595	23
50	2.527105992	5.75617346	23

To evaluate the effect of the reduced vaporization enthalpy by the use of meniscus thin-film evaporation in the hollow fibers of the HCMFs to the evaporation ability, evaporation rate of carbonized cotton microfibers (CCMFs) before water cycling and freeze casting processes was also measured as a comparison.

As seen in Fig. S17, the evaporation rate of HCMFs 2 was 3.2 kg m^{-2} h^{-1}, approximately 33 % higher than that of CCMFs (evaporation rate was calculated to be 2.4 kg m^{-2} h^{-1}). These results demonstrated that the evaporation rate was increased by the capillary hollow fibers in the HCMFs 2. These capillary hollow fibers reduced vaporization enthalpy via meniscus thin-film effect, thus improved evaporation ability.

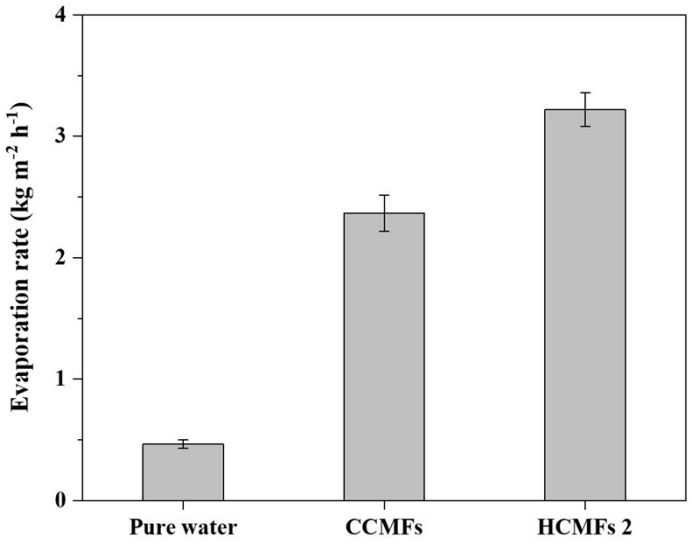

Fig. S17 Under 1 sun evaporation rate of pure water, CCMFs (carbonized cotton fibers without water cycling and freeze-casting processes), and HCMFs 2.

S2.10 Salinities measurement of purified water

Given that in a solution, the value of conductivities that measured by conductivity meter reflected the fact of total dissolved solids (TDS).[7] In this study, salinities were proportional to conductivities, as seen in Fig. S18 the standard saline water with salinities of 0.06%, 0.07%, 0.08%, 0.09%, and 0.10% were prepared, and the corresponding conductivities were measured by a conductivity meter (Acorn CON 6 Series, Oakton Instrument). The salinities and the conductivities were designated as y and x, the liner fitting result showed that $\mathrm{y} = ax$.

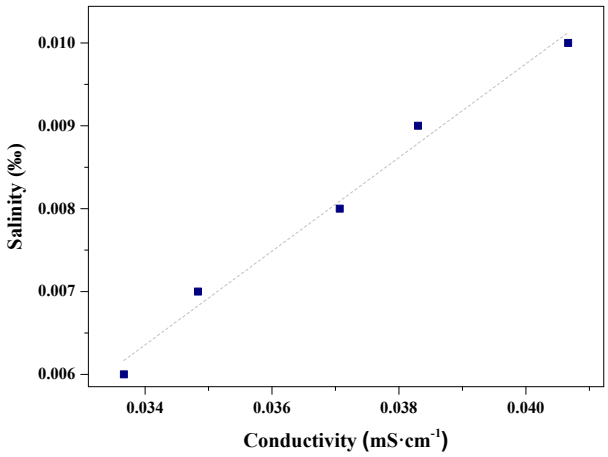

Fig. S18 Liner fitting of salinities of seawater after desalination in the HCMFs.

The conductivities that measured after seawater desalination with initial salinities of 0.8%, 3.5%, and 10% were showed in Table S4, the average conductivities were calculated and plugged into the equation above for salinities calculation of desalted water. After desalination process, all kinds of seawater were purified, the salinities of purified water were significantly decreased below World Health Organization (WHO) and US Environmental Protection Agency (EPA) standards for drinkable water (Fig. 5b), indicating an outstanding desalination performance of the HCMFs solar evaporator.

Table S4. Salinities of seawater before and after desalination

Original salinity (‰)	Conductivity after desalination (mS cm^{-1})			Average conductivity (mS cm^{-1})	Calculated salinity of purified water (‰)
8	0.0295	0.0296	0.0311	0.030	0.004135
35	0.0388	0.0359	0.0363	0.037	0.008054
100	0.0336	0.034	0.0335	0.034	0.006189

S2.11 Non-toxicity of the HCMFs evaporator

As seen in Fig. S19, mean weight of pinto beans was measured during seedling process in this study to evaluate non-toxicity of the HCMFs evaporator. [8-10] Seed weights showed an obvious increasing trend for DI water and the HCMFs desalted water in 3 days and 6 days while the seeds treated with unpurified water exhibited an increasing weight in 3 days, but the weight no longer changed in the 6 days. Because in the first 3 days, the dry seeds absorbed water, leading to an increasing of mean weight, but the seeds were not activated by treating with brine, the weight still remained the same with previous. The results indicated that the HCMFs and the purified water were non-toxic, which was promising for drinkable water supply.

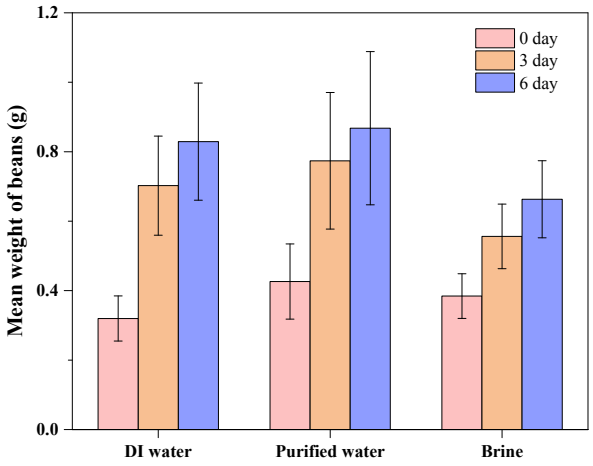

Fig. S19 Mean weight of pinto beans that treated by DI water, HCMFs purified water, and brine, respectively.

S3. Supplementary References

[1] I. Y. Lee, B. R. Evans, J. Woodward, *Ultramicroscopy* **2000**, 82, 213.

[2] *Cotton Fiber: Physics, Chemistry and Biology*, (Ed. D. D. Fang), Springer International Publishing, Cham **2018**.

[3] T. P. Boyer, J. I. Antonov, O. K. Baranova, H. E. Garcia, D. R. Johnson, A. V. Mishonov, T. D. O'Brien, D. Seidov, I. Smolyar, M. M. Zweng, C. R. Paver, R. A. Locarnini, J. R. Reagan, C. Forgy, A. Grodsky, S. Levitus, World Ocean Database 2013, https://www.nodc.noaa.gov/OC5/WOD13/, accessed: September 2013.

[4] H. Liu, Z. Huang, K. Liu, X. Hu, J. Zhou, *Adv. Energy Mater.* **2019**, 9, 1900310.

[5] H. Ghasemi, G. Ni, A. M. Marconnet, J. Loomis, S. Yerci, N. Miljkovic, G. Chen, *Nat. Commun.* **2014**, 5, 4449.

[6] L. Shi, Y. Wang, L. Zhang, P. Wang, *J. Mater. Chem. A* **2017**, 5, 16212.

[7] F. Zhao, X. Zhou, Y. Shi, X. Qian, M. Alexander, X. Zhao, S. Mendez, R. Yang, L. Qu, G. Yu, *Nat. Nanotechnol.* **2018**, 13, 489.

[8] C. Chen, Y. Kuang, L. Hu, *Joule.* **2019**, 3, 683.

[9] N. P. Macdonald, F. Zhu, C. J. Hall, J. Reboud, P. S. Crosier, E. E. Patton, D. Wlodkowic, J. M. Cooper, *Lab Chip* **2016**, 16, 291.

[10] Y. Luo, J. Liang, G. Zeng, M. Chen, D. Mo, G. Li, D. Zhang, *Waste Manage.* **2018**, 71, 109.